Revealing the corrosion mechanism of an Al0.1CoCrFeNi high entropy alloy in high temperature carbon dioxide environment

Zhou, Shanliang
Liang, Zihang
Huang, Xi
Xia, Yuxuan
Zhao, Qi
Cheng, Chun
Zhu, Pengcheng
Wu, Lu
Xie, Yujun

To be published in: Corrosion Science

DOI to publisher's version: 10.1016/j.corsci.2024.112411

Revealing the corrosion mechanism of an $Al_{0.1}CoCrFeNi$ high entropy alloy in high temperature carbon dioxide environment

Shanliang Zhou, Zihang Liang, Xi Huang, Yuxuan Xia, Qi Zhao, Chun Cheng, Pengcheng Zhu, Lu Wu, Yujun Xie

PII: S0010-938X(24)00606-1

DOI: https://doi.org/10.1016/j.corsci.2024.112411

Reference: CS112411

To appear in: *Corrosion Science*

Received date: 9 June 2024
Revised date: 16 August 2024
Accepted date: 23 August 2024

Please cite this article as: Shanliang Zhou, Zihang Liang, Xi Huang, Yuxuan Xia, Qi Zhao, Chun Cheng, Pengcheng Zhu, Lu Wu and Yujun Xie, Revealing the corrosion mechanism of an $Al_{0.1}CoCrFeNi$ high entropy alloy in high temperature carbon dioxide environment, *Corrosion Science,* (2024) doi:https://doi.org/10.1016/j.corsci.2024.112411

Revealing the corrosion mechanism of an $Al_{0.1}CoCrFeNi$ high entropy alloy in high temperature carbon dioxide environment

Shanliang Zhou [a, b,1], Zihang Liang [b,1], Xi Huang [a, b, *], Yuxuan Xia [a], Qi Zhao [a, b], Chun Cheng [c], Pengcheng Zhu [d], Lu Wu [e, *], Yujun Xie [b, *]

[a] School of Nuclear Science and Engineering, East China University of Technology, Nanchang, Jiangxi 330013, China

[b] Global Institute of Future Technology, Shanghai Jiao Tong University, Shanghai 200240, China

[c] Instrumental Analysis Center, Shanghai Jiao Tong University, Shanghai 200240, China

[d] Los Alamos National Laboratory, Los Alamos, NM 87547, USA

[e] Nuclear Power Institute of China, Chengdu, Sichuan 610041, China

*Corresponding author.

E-mail address: xihuang@ecut.edu.cn (Xi Huang)

wulu1002@126.com (Lu Wu)

yujun.xie@sjtu.edu.cn (Yujun Xie)

[1] These authors contributed equally to this work.

ABSTRACT

The corrosion behavior of an $Al_{0.1}CoCrFeNi$ HEA in high temperature CO_2 at 850 °C for different exposure periods was investigated using different characterization methods. Weight gain increased with extended exposure periods, yet it remained lower than most conventional alloys. A double-layer oxide film consisting of Cr_2O_3 and Al_2O_3 formed after 100 and 500 h of exposure, while a single layer of Cr_2O_3 developed after 1000 h of exposure. CoCrFeNi particles with an FCC structure were embedded in the oxide films irrespective of the exposure periods. Moreover, a transition zone containing numerous striped-like Al_2O_3 oxides along the grain boundaries was developed underneath the oxide films.

Keywords: High entropy alloys; High temperature CO_2; Corrosion behavior; Oxide films; Al_2O_3

1. Introduction

As the global economy continues to expand rapidly, there is a corresponding surge in the consumption of fossil fuels, leading to a significant amount of carbon dioxide (CO_2) emissions in the air, which causes environmental problems [1]. Carbon capture and storage is a solution for reducing CO_2 emission, which involves capturing and storing CO_2 emissions from burning fossil fuels or other industrial processes [2,3]. Currently, a new technology, known as oxy-fuel combustion, has been developed, in which coal is combusted within a mixture of oxygen and recirculated flue gas [4]. Consequently, the flue gas, composed of CO_2 and water vapor, is emitted, presenting an easy opportunity for CO_2 gas sequestration. In addition, the supercritical CO_2 (S-CO_2) Brayton cycle is being evaluated for power conversion in advanced nuclear power plant applications because of its superior efficiency and compactness compared to traditional steam cycles [5]. Nonetheless, these advanced technologies can potentially exacerbate the corrosion issues of materials used in power plants [6].

At present, the corrosion behavior of conventional alloys, such as ferritic-martensitic (F-M) steels, nickel-based alloys, austenitic stainless steels, chromia-forming steels, and so on, is being meticulously evaluated under high temperature conditions, especially for CO_2 environment [4,7–10]. However, most conventional alloys will suffer severe corrosion, making them unsuitable for use in these advanced systems. For instance, ferritic-martensitic steels commonly exhibit severe oxidation and carburization behavior in high temperature CO_2 environments [10–12]. Under such an atmosphere, most austenitic stainless steels experience breakaway oxidation and carburization behavior [8,13]. The same corrosion behavior is observed in chromia-forming steels after exposure to the same environment [9,14,15].

Recently, a new class of alloys named high entropy alloys (HEAs) with a unique combination of mechanical, physical, and chemical properties, including high ductility, hardness, creep strength, stability of the microstructure, and excellent corrosion resistance, has been developed by Yeh *et al.* [16–20]. These superior properties make HEAs a prominent candidate material for advanced power plants. However, only two references reported the corrosion behavior of HEAs under high temperature CO_2 environments [21,22]. Thorhallsson *et al.* studied the corrosion behavior of CoCrNiFeMo and CoCrNiFeMoCu HEA tested in a simulated superheated geothermal environment at 350 ℃ and 10 bar gauge containing HCl, H_2S, and CO_2 with acidic condensate (pH = 3) and reported that the addition of Cu devastated the corrosion resistance of HEAs [21].

The corrosion behavior of an equimolar FeCoNiCrMn HEA in various combinations of CO_2/CO mixed gases at 700 and 950 ℃ was investigated by Kai *et al.*, and reported that at 700 ℃, a thin layer consisting of a mixture of MnO, $(Mn,Fe)_3O_4$, and $(Mn,Cr)_3O_4$ was formed on the HEA, while a duplex scale was observed at 950 ℃, comprising an outer layer of $(Mn,Fe)_3O_4$ and MnO, and an inner layer of $(Mn,Cr)_3O_4$ and MnO [22]. The results of the above investigations indicated that the chemical compositions and microstructures of HEAs, along with environmental factors, are pivotal determinants of the corrosion behavior of HEAs in high temperature CO_2 environments. However, there remains a lack of insight into how these factors affect the corrosion behavior of HEAs.

Compared to FeCoNiCr HEA system, the $Al_xCoCrFeNi$ HEA system exhibits superior mechanical performance and corrosion resistance [23–25], drawing considerable attention to this alloy. Currently, the microstructure and mechanical properties of $Al_xCoCrFeNi$ HEAs have been evaluated because of the phase transformation from face-centered-cubic (FCC) to body-centered cubic (BCC) crystal structure as the Al concentration increases [26–28]. Additionally, extensive studies on the oxidation behavior of the $Al_xCoCrFeNi$ HEAs system in high temperature air conditions have revealed exceptional corrosion resistance, especially at high Al concentrations [29–32]. The superior properties of this HEA make it highly recommended for future industrial applications [33], especially for advanced power plants. However, the corrosion behavior and mechanism of this series of HEAs in high-temperature CO_2 are still poorly understood. This study aimed to investigate the corrosion behavior and mechanism of an $Al_{0.1}CoCrFeNi$ HEA in a high temperature CO_2 environment with different exposure periods. The reasons for selecting $Al_{0.1}CoCrFeNi$ HEA as a model alloy are as follows: (a) its microstructures and mechanical properties are well-documented; (b) a simple FCC single phase makes it easier to study fundamental mechanisms; and (c) its outstanding mechanical properties make it a promising system for various applications. The corrosion products were identified by X-ray diffraction (XRD), and the chemical composition and structure of the oxides were characterized by scanning electron microscopy (SEM), transmission electron microscopy (TEM), and Time-of-Flight Secondary Ion Mass Spectrometry (ToF-SIMS).

2. Experimental procedures

2.1 Materials and corrosion test samples

The $Al_{0.1}CoCrFeNi$ HEA was prepared using an induction melting furnace under a controlled argon atmosphere to prevent oxidation. Iron (Fe), cobalt (Co), nickel (Ni), chromium (Cr), and aluminum (Al), each with purities exceeding 99.9 wt.%, were utilized as raw materials. The ingots were remelted at least five times to homogenize the chemical composition. The nominal composition of this alloy was measured by an SEM of Nova Nano SEM 450 equipped with an OXFORD Instrument INCA energy X-ray dispersive spectroscope (EDS). The measurement revealed the following composition in atomic percent (at. %): 24.05% Cr, 25.21% Ni, 23.53% Fe, 2.79% Al, and 24.42% Co.

Samples measuring $10 \times 10 \times 3$ mm^3 were cut from the as-cast $Al_{0.1}CoCrFeNi$ HEA to conduct the corrosion experiments. A hole with a diameter of 2 mm was drilled at the upper part of the samples to suspend them on an Al_2O_3 rod with a diameter of 0.5 mm. Each of these samples was ground progressively with silicon carbide sandpaper up to 2000 # grit, then cleaned with acetone, and ultrasonically rinsed with ultrapure water for 10 mins prior to the tests. At least three samples were exposed to high temperature CO_2 each time.

2.2 High temperature CO_2 exposure test

Isothermal corrosion tests were conducted in a CO_2 environment at 850 ℃ for 100, 500 and 1000 h. Fig. 1 illustrates a schematic of the CO_2 corrosion test facility used in the current investigations. The maximum operating temperature for this facility is 1600 ℃ at 0.1 MPa. A research-grade CO_2 gas (99.99% purity with less than 1 ppm of O_2 and H_2O) was employed to conduct the corrosion experiments.

2.3 Microstructural analysis

After the corrosion experiments, the CO_2 corrosion test facility was cooled to room temperature (RT), and the samples were subsequently removed. The weight gain was measured using a D&T ES1055A microbalance with a resolution of 0.001 mg before and after the corrosion experiments. The crystalline phases of the as cast $Al_{0.1}CoCrFeNi$ HEA and the oxide phases formed on the $Al_{0.1}CoCrFeNi$ HEA after the corrosion experiments were identified by a D8 Advance X-ray diffraction (XRD) using Cu-k_α radiation at 30 kV and 50 mA, with a scanning rate of 2° per minute between 10° and 90°. The initial microstructure and chemical composition of the as-cast $Al_{0.1}CoCrFeNi$ HEA were comprehensively analyzed using a Nova Nano SEM 230 equipped with electron backscattered diffraction (EBSD) and EDS. SEMs, including JSM-7800F, Nova Nano

SEM 450, and 230 equipped with EDS, were employed to characterize the morphologies and compositions of the surface oxide films in both plan and cross-sectional views of the samples.

The TEM lamellas were prepared from cross-sectional views of the samples using a Helios 5 CX dual beam focused ion beam (FIB). A protective platinum layer was deposited on the oxide film at 30 kV and a current of 0.04 nA. FIB trenches were made using 30 kV and a high current of 21 nA for rough milling. Cross-sections were fine milled using a current of 9.3 nA. After lifting out the sample with an Easylift needle and welding it to a Cu TEM grid, the lamellas were thinned down with 30 kV at 2.5 nA. During the thinning down, the operating voltage and current were subsequently reduced until 8 kV and 23 pA, respectively. An FEI Talos-F200X TEM, operated at 200 kV and equipped with an EDS detector, was utilized to characterize and image the samples. TEM-EDS was performed on cross-sections of the oxide films to determine the chemical composition. The selected area electron diffraction (SAED) patterns and fast Fourier transform (FFT) analyses were employed to determine the crystal structure of the oxides.

In addition to SEM and TEM, an ION TOF Time-of-Flight Secondary Ion Mass Spectrometry (ToF-SIMS) 5-100 was employed to further characterize the elemental depth profiles of the oxides developed on $Al_{0.1}CoCrFeNi$ HEA after different exposure periods. All ToF-SIMS measurements were performed under a pressure lower than $\sim 10^{-9}$ mbar, with careful control of primary ion doses to prevent surface contamination during in-depth profiling and maintain static conditions. A pulsed 30 keV Bi^+ primary ion source, delivering 0.5 pA over an area of 10×10 μm², was used for analysis. Depth profiling was conducted by interlacing static analysis with sputtering using a 2 keV Cs^+ sputter beam giving a 110 nA target current over a 100×100 μm² area. Data acquisition and processing were performed using the IonSpec software.

3. Results

3.1 Initial microstructure

The initial microstructure of the as-cast $Al_{0.1}CoCrFeNi$ HEA is displayed in Fig. 2. The XRD pattern of Fig. 2 (a) indicated that all diffraction peaks corresponded to an FCC structure with lattice parameters of $a = b = c = 3.638$ Å. A substantial number of grains, each with a width of several millimeters, were observed in the SEM-EBSD image displayed in Fig. 2 (b), indicating the formation of a polycrystalline microstructure. The SEM-EDS mapping images illustrated in Fig. 3 revealed that no chemical segregation occurred in this HEA. These results are consistent with the previous investigations on the microstructure of the as-cast $Al_{0.1}CoCrFeNi$ HEA [34,35].

3.2 Corrosion kinetics

Fig. 4 shows the relationship between weight gain and exposure time for $Al_{0.1}CoCrFeNi$ HEA and other alloys in high temperature CO_2 at 850 ℃. The weight gain increased gradually with the exposure time, regardless of the chemical composition of the alloys. The following equation (1) can be employed to fit experimental data and describe the corrosion process [13]:

$$\Delta W = kt^n \quad (1)$$

Where ΔW is the weight gain before and after corrosion experiments, t is the exposure period, k is the rate constant, and n is the reaction order. The fitting results indicated that corrosion kinetics approximately followed the parabolic law ($n=0.5$) for $Al_{0.1}CoCrFeNi$ HEA ($n=0.425$), as shown in Fig. 4 (b), representing a diffusion-controlled oxide growth rate [13]. This implied that the formation of the oxide films was determined by the diffusion rate of elements or gas molecules. For instance, the outward diffusion of metal elements from the matrix through the oxide layer to the scales/gas interface produced corresponding oxides on the outermost surface [13,36]. Meanwhile, the inward transport of gas molecules favored the growth of the inner layer [37]. However, the weight gain of 316L stainless steel (SS) ($n=0.354$) deviated from the parabolic law, attributed to sporadic spallation of the oxide layer. The weight gain of $Al_{0.1}CoCrFeNi$ HEA and other nickel-based alloys, such as 230, 617, and 203 [38], obtained from similar exposure conditions was illustrated in Fig. 4 (b). The results revealed that the corrosion resistance of $Al_{0.1}CoCrFeNi$ HEA was better than that of 601 and 617 alloys in a high-temperature CO_2 environment at 850 ℃, with a slightly higher than that of 203 alloys. This result further demonstrated that the corrosion resistance behavior of $Al_{0.1}CoCrFeNi$ HEA is better than most of conventional alloys under similar corrosion conditions.

3.3 XRD analysis

The XRD analysis results of the surface oxides formed on $Al_{0.1}CoCrFeNi$ HEA corroded in high temperature CO_2 at 850 ℃ for 100, 500, and 1000 h are illustrated in Fig. 5. In addition to the peaks originating from the FCC matrix (JCPDS 52-0513), peaks at 24.35°, 33.54°, 36.05°, 41.34°, 49.93°, 54.85°, 58.06°, 63.15°, and 64.75° were observed after exposure to high temperature CO_2 for 100, 500, and 1000 h, indicating the formation of Cr_2O_3 (JCPDS 38-1479) during those exposure periods. In addition to Cr_2O_3, peaks at 18.21° and 30.25° were corresponded to the formation of Fe_2O_3 (JCPDS 40-1139) as the exposure periods increased to 1000 h, presenting the formation of Fe_2O_3. Furthermore, the intensity of Cr_2O_3 peaks after 1000 h of exposure was

significantly higher than that of samples exposed for 100 and 500 h, suggesting further growth of Cr_2O_3.

3.4 Surface oxide morphologies

Fig. 6 displays the SEM images of $Al_{0.1}CoCrFeNi$ HEA after exposure to high-temperature CO_2 at 850 °C for different testing periods. Following 100 h of exposure, a large number of irregular oxide particles were observed on the surface of the samples. Moreover, the density of oxides on scratches was higher than in areas away from the scratches, as shown in Fig. 6 (a) and (d). The SEM-EDS results in Table 1 and Fig. S1 (Supporting Information) revealed that these irregular oxide particles were Cr-rich oxides. Combining these findings with XRD results, it can be inferred that these Cr-rich oxides are Cr_2O_3. The irregular oxide particles gradually covered the surface of the HEA as the exposure time increased from 500 to 1000 h, as shown in Fig. 6 (b) and (c). These oxide particles were identified as Cr_2O_3 based on the SEM-EDS analysis shown in Table 1, Fig. S2, and Fig. S3. Furthermore, the Cr_2O_3 particles gradually aggregated and formed petal-shaped Cr_2O_3 oxides, as illustrated in Fig. 6 (e) and (f). These results indicated that the surface oxide morphologies of the samples evolved with increased exposure periods, while the chemical composition of the oxides remained stable.

3.5 Cross-sectional oxide film analysis

The cross-sectional SEM images and the results of EDS mapping and line analysis of the $Al_{0.1}CoCrFeNi$ HEA after exposure to high temperature CO_2 at 850 °C for 100, 500, and 1000 h were illustrated in Fig. 7. The results of SEM images and corresponding EDS mapping revealed that a double-layer oxide film, consisting of an outer Cr-rich layer and an inner Al-rich layer, formed on $Al_{0.1}CoCrFeNi$ HEA after 100 and 500 h, while a single layer of Cr-rich oxide film developed after 1000 h of exposure. Furthermore, the thickness of the oxide films increased with increasing exposure periods. It was 0.66 ± 0.28 μm after 100 h, 0.98 ± 0.22 μm after 500 h, and 1.82 ± 0.14 μm after 1000 h, as evidenced by the line scan analysis of the HEA. Besides, it is interesting to note that a transition zone containing a large number of striped-like Al-rich oxides was formed underneath the oxide films following various exposure periods. The thickness of this transition zone increased with prolonged exposure periods. It was 2.85 ± 0.58 μm after 100 h, 5.15 ± 1.18 μm after 500 h, and 6.71 ± 1.27 μm after 1000 h.

Fig. 8 shows the ToF-SIMS negative ion depth profiles for the oxide films developed on the surface of the $Al_{0.1}CoCrFeNi$ HEA after exposure for different periods. The intensity is plotted in

logarithmic scale versus sputtering time. Variations in intensity with the sputtering time on the profile indicate changes in in-depth concentration. The CrO_2^- ion profile was employed to define the outer oxide layer region, ending at 84% of the maximum depth profile intensity, owing to the duplex structure of the oxide film with a Cr-rich outer layer [39,40]. The Ni_2^- ion profile was utilized to define the metallic region, starting at the beginning of the intensity plateau [39]. The red dashed lines mark the boundaries between the outer oxide film, the inner oxide film, and the metallic substrate.

In the oxide region, the profile peaks of FeO_2^-, NiO_2^-, and CoO_2^- appeared on the surface of the oxide film region and gradually decreased through the oxides. Therefore, oxidized Fe, Ni, and Co are predominantly developed on the out layer of the oxide films. The CrO_2^- exhibited its maximum intensity in the outer layer of the oxide films, suggesting that Cr-rich oxide was the primary species, as shown in Fig. 8. Additionally, the presence of other peaks (FeO_2^-, AlO_2^-, CoO_2^-, and NiO_2^-) indicated that the outer oxide layer was not a pure oxide but a mixed oxide composed of these alloy elements. Regarding the inner oxide layer, the single intensity of metallic compounds (Al_2^-, Ni_2^-, Cr_2^-, Co_2^-, and Fe_2^-) gradually increased while the characteristic signals of the oxides decreased rapidly. The intensity of AlO_2^- was notably higher than that of other oxides, regardless of exposure time. Furthermore, after 1000 h oxidation, the AlO_2^- depth profile closely resembles those of metallic elements, suggesting that the majority of Al_2O_3 is located in the substrate region. In addition, the results presented in Fig. 8 revealed that there was minimal alteration in the chemical composition and structure of the oxide films over the extended exposure periods, except for an increase in thickness. Based on ToF-SIMS observations, it is established that a duplex oxide structure consisting of a Cr-rich outer layer and an Al-rich inner layer formed on samples after 100 and 500 h of exposure, while a single layer of Cr_2O_3 developed after 1000 h of exposure. This result is similar to the results obtained from SEM-EDS, as shown in Fig. 7.

Fig. 9 shows the TEM analysis of the cross-section of the oxide films developed on $Al_{0.1}CoCrFeNi$ HEA after 100 h of exposure. The high-angle annular dark-field (HAADF) scanning transmission electron microscopy (STEM) image and corresponding EDS mapping results revealed the formation of a double-layer of oxide film, consisting of a Cr-rich outer layer and an Al-rich inner layer, as shown in Fig. 9 (a). The Cr-rich outer layer was identified as $(Cr_{0.83}Al_{0.01}Fe_{0.06}Co_{0.01}Ni_{0.09})_2O_3$ based on the FFT pattern and TEM-EDS, and the Al-rich inner layer was identified as $(Al_{0.72}Cr_{0.8}Fe_{0.04}Co_{0.04}Ni_{0.12})_2O_3$, as illustrated in Fig. 9 (b). Further analysis

revealed that the Cr_2O_3 film was composed of columnar particles approximately 58.4 ± 17.5 nm in size, as shown by the yellow arrows in Fig. 9 (c). The Cr_2O_3 and Al_2O_3 oxide layer thickness was 0.81 and 0.14 μm, respectively, as displayed in Fig. 9 (b). The thin layer of Al_2O_3 developed underneath Cr_2O_3 may be due to the lower concentration of Al in $Al_{0.1}$CoCrFeNi HEA. A transition zone containing a large number of striped-like Al-rich oxides was formed underneath the oxide films, as shown in Fig. 9 (a), in line with the results of SEM images illustrated in Fig. 7. The results of the FFT pattern and TEM-EDS illustrated in Fig. 9 (d) confirmed that these oxides were identified as $(Al_{0.72}Cr_{0.8}Fe_{0.04}Co_{0.04}Ni_{0.12})_2O_3$. Furthermore, these oxides were formed along the grain boundaries, as illustrated in Fig. 9 (a), suggesting that the inward diffusion of CO_2 promoted the formation of Al_2O_3. In addition, it is interesting to find some CoCrFeNi particles with an FCC structure embedded in the oxide film, as displayed in Fig. 9 (a) and (e).

TEM analysis of the cross-section of the oxide films developed on $Al_{0.1}$CoCrFeNi HEA after 1000 h of exposure was illustrated in Fig. 10. The average size of the CoCrFeNi particles and Cr_2O_3 grains increased significantly compared to the samples after 100 h of exposure, as illustrated in Fig. 10 (a) and (c). In addition to the size of CoCrFeNi particles and Cr_2O_3 grains, slight differences in the chemical composition and structure of the oxide films were observed after comparing the samples exposed for 100 h, as illustrated in Fig. 10 (b) to (f). A monolayer of $(Cr_{0.95}Al_{0.01}Fe_{0.02}Co_{0.01}Ni_{0.01})_2O_3$ rather than a double-layer of oxide film was developed on $Al_{0.1}$CoCrFeNi HEA. The thicknesses of this Cr_2O_3 layer were 1.41 μm, exceeding those observed in the sample after 100 h of exposure, as shown in Fig. 10 (b). This result indicated that the thickness of the oxide films gradually increased with extended exposure periods, consistent with the findings presented in Fig. 7 and 8. The EDS line analysis revealed no significant difference in carbon concentration underneath the oxide film, as illustrated in Fig. 9 and 10, implying that there was no significant carbon diffusion to the matrix even though the exposure periods extended to 1000 h. Additionally, SEM and TEM results revealed the formation of a mixed oxide film composed of Cr_2O_3 and Al_2O_3 on the surface of this alloy. In contrast, XRD patterns indicated the presence of a mixed oxide film consisting of Cr_2O_3 and Fe_2O_3. The absence of peaks associated with Al_2O_3 in the XRD spectrum can be attributed to two factors. Firstly, the Al_2O_3 layer was too thin to be detected by XRD compared to the Cr_2O_3 layer. For instance, after 100 h of exposure, the thickness of the Cr_2O_3 layer was approximately 0.72 μm, while the thickness of the Al_2O_3 layer was 0.08 μm, as shown in Fig. 9. Secondly, no Al_2O_3 layer was formed on the surfaces of the

samples after oxidation. For example, only a monolayer of Cr_2O_3 was observed after 1000 h of exposure, as shown in Fig. 10. In addition, the quantity of Fe_2O_3 on the surface of alloys is so low that it is challenging for SEM and TEM to detect easily.

4. Discussion

4.1 Corrosion mechanism

In high-temperature CO_2 environments, oxidation of $Al_{0.1}CoCrFeNi$ HEA begins with the immediate combination of CO_2 molecules with the metal atoms on the surface. This interaction triggers a series of chemical reactions, leading to the formation of corresponding oxides, as described by the following equations [7,10,41,42]:

$$2Al + 3CO_2(g) \rightarrow Al_2O_3 + 3CO(g) \quad (2)$$

$$2Cr + 3CO_2(g) \rightarrow Cr_2O_3 + 3CO(g) \quad (3)$$

$$3Fe + 4CO_2(g) \rightarrow Fe_3O_4 + 4CO(g) \quad (4)$$

$$Ni + CO_2(g) \rightarrow NiO + CO(g) \quad (5)$$

$$Co + CO_2(g) \rightarrow CoO + CO(g) \quad (6)$$

The order of Gibbs formation energy of these oxides is $\Delta G(Al_2O_3) < \Delta G(Cr_2O_3) < \Delta G(Fe_3O_4) < \Delta G(NiO) < \Delta G(CoO)$ [43]. This result indicates that the formation of Al_2O_3 is thermodynamically favorable, leading to its preferential formation on the surface of HEA during the initial stage of corrosion. Nevertheless, the lower Al concentration in the $Al_{0.1}CoCrFeNi$ HEA (2.74 wt. %) is inadequate to support the formation of a continuous Al_2O_3 layer. Consequently, a discontinuity Al_2O_3 layer is formed, as confirmed by Fig. 9 and 10.

The oxidation process of $Al_{0.1}CoCrFeNi$ HEA in this high-temperature CO_2 environment involves the diffusion and subsequent combination of external CO_2 molecules with the metal atoms within the matrix [4,44]. Upon exhaustion of the easily oxidizable Al elements on the surface of the substrate, the internal metal elements, for example, the Cr element, undergo diffusion to the exterior, thereby contributing to the subsequent oxidation behavior [45,46]. The diffusion coefficient of Cr in $Al_{0.1}CoCrFeNi$ HEA is greater than that of Al [47], enabling Cr to diffuse outward more rapidly than Al and react with CO_2 to form Cr_2O_3. Furthermore, the formation of a discontinuous Al_2O_3 layer on the surface of HEA is insufficient to prevent the outward diffusion of Cr from the matrix. Cr can continuously diffuse outward through the Al_2O_3 oxide film, forming a Cr_2O_3 layer. Additionally, the critical Cr concentration requires to form and sustain a protective

Cr_2O_3 layer decreased at higher temperatures due to the enhanced diffusion of Cr within the HEA [4]. Therefore, the thickness of this oxide film progressively increases over time, as illustrated in Fig. 7 and 8.

Concurrently, CO_2 gas molecules continue to diffuse into the interior of the $Al_{0.1}$CoCrFeNi HEA along the grain boundaries, penetrating the region beneath the existing oxide layer. Al preferentially reacts with CO_2 due to its thermodynamic favorability [48], forming numerous striped Al_2O_3 particles along the grain boundaries, as shown in Fig. 7. Additionally, the formation of the Al_2O_3 layer consumes a significant portion of Al, further reducing the Al content in the substrate underneath this oxide layer, as displayed in Fig. 11. These results lead to a lower concentration of Al in the matrix than the critical value required to initial the formation of the Al_2O_3 oxide layer [49]. Therefore, Al_2O_3 particles are developed along the grain boundaries rather than oxide film. With the increase in exposure periods, CO_2 gradually diffuses into the matrix along the grain boundaries, leading to a gradual increase in the thickness of the transition layer. The formation of Al_2O_3 particles induces compressive stress on adjacent grains, prompting the metal to extrude outward along grain boundaries. This phenomenon culminates in the formation of CoCrFeNi particles within the Cr_2O_3 oxide films.

4.2 Formation of CoCrFeNi particles

Current results revealed that regardless of exposure periods, CoCrFeNi particles with an FCC structure were embedded in the oxide films, as shown in Fig. 9 and 10. The main chemical compositions and structure of these particles were consistent with the metallic matrix (Al-depleted FCC solid solution substrate layer) underneath the oxide films. However, the Al concentration in these particles was significantly lower than the content in the matrix, as shown in Fig. 11. The former was 0.28 at. %, while the latter was 2.74 at. %. These results significantly differed from the previous investigations on the corrosion behavior of the conventional alloys under high temperature CO_2, especially for alloys with varying Al concentrations [50–53]. The most significant disparity between these two types of alloys stemmed from their chemical compositions. Conventional alloys typically consist of one primary metallic element with varying properties, whereas HEAs contain at least five elements in equal or approximately equal atomic proportions [54,55]. Therefore, the formation of CoCrFeNi particles originated from the differences in chemical compositions within the matrix. The differences in chemical composition and

concentration resulted in the formation of various oxides on $Al_{0.1}CoCrFeNi$ HEA, which ultimately influenced the formation of CoCrFeNi particles.

Our current findings demonstrated that a duplex-layer oxide film was developed on $Al_{0.1}CoCrFeNi$ HEA after exposure to high temperature CO_2 for different periods, including a Cr_2O_3 external oxide layer and a discontinuous Al_2O_3 internal oxide layer, as displayed in Fig. 7-10. The formation of an internal discontinuous Al_2O_3 layer, particularly the internal Al_2O_3 particles along the grain boundaries, usually increased in the volume of the samples [56,57]. The volume increase associated with Al_2O_3 formation inevitably generated stress at the interface between the internal oxidation front and within the internal oxidation zones [56]. The following equation can be employed to predict the type of stress (compressive stress or tensile stress) developed in the oxide scales during the oxidation process [58]:

$$PBR_{HEA} = \frac{V_{Al_2O_3}}{V_{HEA}} = \frac{M_{Al_2O_3} \times \rho_{HEA}}{2 \times M_{HEA} \times \rho_{Al_2O_3}} \quad (7)$$

where *PBR* is the Pilling-Bedworth ratio of $Al_{0.1}CoCrFeNi$ HEA, *M* is the molecular or atomic mass, *V* is the molar value, and ρ is the density. Utilizing the value of corresponding parameters in references [27,58,59], the *PBR* value of $Al_{0.1}CoCrFeNi$ HEA can be calculated to be 3.94, which exceeds 1.0. It is generally accepted that compressive stress develops in the oxide scale when *PBR* is greater than 1, while tensile stress corresponds *PBR* less than 1 [60]. Therefore, compressive stress would be generated between the Al_2O_3 and matrix. As exposure periods increased, compressive stress accumulated and eventually necessitated relief in some manner. Four main stress relief mechanisms were proposed based on the results obtained from different alloys. F.H. Stoot *et al.* investigated the intergranular oxide behavior of Ni-Al alloys at different temperatures and proposed that stress in the Ni-Al systems was relieved by intergranular oxidation, grain boundary sliding, and extrusion of weak, internal oxide-denuded zones adjacent to grain boundaries [57,61]. Besides, J.A. Nychka *et al.* studied the oxidation behavior of FeCrAlY alloys in a high temperature air environment and proposed that the evolving compressive growth stress in the oxides led to grain sliding, resulting in the formation of cracks and spalls at the edges of the uplifted grains [62]. G.C. Wood *et al.* investigated the same alloy systems (NiCrAl) at high temperatures and proposed that metal flow within the grains relieved stress in the Ni-Cr systems [63]. J.R. Mackert *et al.* studied the oxidation behavior of a Pd-Ag-based alloy at high temperatures and proposed outward transport of the base metal as a stress relief mechanism [64]. In addition,

other investigations on the oxidation behavior of Ag-In alloy, Pb-Ag alloy, and Ni-Al alloys suggested that dislocation pipe diffusion was responsible for transporting metallic elements to the surface of the samples [64–66]. In current investigations, no noble metal elements existed in this HEA. Furthermore, no dislocations were observed around the CoCrFeNi particles, as illustrated in Fig. 9 and 10. Previous investigations have confirmed that the flow of metal within grains occurred easily for dilute binary alloys, facilitating the formation of single-phase scales, while it seemed unlikely to occur for ternary alloys [65]. These results suggested that dislocation pipe diffusion, the flow of metal within the grains, and outward transport of the base metal were not the stress relief mechanisms for $Al_{0.1}$CoCrFeNi HEA exposed to this high-temperature CO_2 environment. It seems that the stress relief mechanisms for $Al_{0.1}$CoCrFeNi HEA under this exposure condition were the intergranular oxidation, grain boundary sliding, and extrusion of weak, internal oxide-denuded zones adjacent to grain boundaries. The TEM image in Fig. 10 indicated that CoCrFeNi particles were separated by an Cr_2O_3 oxide film. The two parts can fit together perfectly if the Cr_2O_3 oxide layer was removed. These results further confirmed the above inferences about the stress relief mechanism for $Al_{0.1}$CoCrFeNi HEA.

The TEM-EDS mapping results suggested that Al_2O_3 particles were formed along the grain boundaries, especially for the grains approaching the surface region of the samples, as shown in Fig. 9 and 10. The volume increase associated with Al_2O_3 formation produced compressive stresses around the grain boundaries. Relieving the compressive stress was difficult due to the effect of the size and distribution of the Al_2O_3 particles [67]. However, sliding oblique grain boundaries under shear stress can achieve a certain degree of compressive stress relief [68]. Furthermore, previous investigations on the oxidation behavior of FeCrAlY alloy in high-temperature air have confirmed that the grains slid during oxidation rather than during the cooling process [62]. The number of Al_2O_3 particles gradually increased as the exposure periods increased, and then the compressive stress gradually accumulated [69]. The value of the reported compressive stress caused by the formation of Al_2O_3, sometimes referred to as the lateral growth stress, ranged from ~1.5 GPa for FeCrAlY alloys to peak values of ~4.4 GPa for the AlCoCrFeNi HEA [62,70]. The compressive stress in the growing Al_2O_3 must be balanced by the tensile stress in the HEA to maintain mechanical equilibrium during oxidation. The higher tensile stress would induce plastic deformation of the grains to relieve stress, especially for the oblique grain boundaries [68]. The oxide films would deform to relieve the compressive stress around the oblique grain boundaries,

resulting in the metal being extruded outward along the grain boundaries, producing CoCrFeNi particles within the Cr_2O_3 oxide films.

4.3 Formation of Al_2O_3 particles

The formation of Al_2O_3 particles underneath the Cr_2O_3 outer oxide layer was determined by the exposure temperature and chemical composition of the HEAs. Concerning exposure temperature, previous investigations on the corrosion behavior of conventional alloys suggested that the higher exposure temperature promoted the formation of Al_2O_3 particles rather than Al_2O_3 films [38,52,71,72]. A continuous or discontinuous Al_2O_3 oxide layer between the outer layer and matrix was developed on alloys at exposure temperatures less than 650 ℃. For instance, L. Tan *et al.* studied the corrosion behavior of alloy 800 H exposed to S-CO_2 at 650 ℃ for 500 h and revealed the formation of a continuous ultra-thin Al_2O_3 layer between the outer layer and the matrix [72]. The same result was reported by G.O. Subramanian *et al.*, who investigated the corrosion behavior of alumina-forming heat resistant alloys in an S-CO_2 environment [52]. He *et al.* investigated the corrosion behavior of an alumina forming austenitic (AFA) steel exposed to an S-CO_2 environment at different temperatures and reported that continuous Al_2O_3 scales were developed on AFA steel at 550 ℃ after short exposure, while some Al_2O_3 particles were formed at the interface between outer oxide scales and matrix after exposure to S-CO_2 at 650 ℃ [71]. Many Al_2O_3 particles were observed underneath the outer layer as the exposure temperature increased to 750 and 850 ℃. Li *et al.* investigated the corrosion behavior of different Ni-based alloys in CO_2 gas at 750 and 850 ℃ and reported that some scatter Al-rich oxide particles tended to penetrate deeper into the matrix of 617 alloy at the exposure temperature of 750 ℃ [38]. Furthermore, as the exposure temperature increased to 850 ℃, the Al-rich oxide particles were more significant in size than particles formed at 750 ℃ and penetrated deeper into the matrix.

It is generally accepted that internal oxidation is a diffusion-controlled process, especially for forming different oxide particles [73]. In the current experiments, CO_2 molecules were absorbed onto the surface of the $Al_{0.1}$CoCrFeNi HEA and then diffused inward to initiate a reaction with the alloying element Al present in the HEA. This reaction led to the formation of Al_2O_3 particles and the subsequent depletion of alloying Al from the matrix, as depicted in Fig. 7-11. The higher the exposure temperature, the faster the nucleation rate of Al_2O_3 particles in the matrix along the grain boundaries [74,75]. Furthermore, increasing exposure temperatures decreased the critical Al concentration to form Al_2O_3 particles [38]. All these results suggested that increasing exposure

temperatures promoted the formation of Al_2O_3. In addition to the formation kinetics of Al_2O_3 particles being affected by exposure temperatures, the depth of Al_2O_3 along the grain boundaries was also influenced by exposure temperatures. The depth of oxide particles, assumed as X, can be calculated according to parabolic kinetics [76]:

$$X^2 = k_p t \quad (8)$$

$$k_p = \frac{\varepsilon D_O N_O^{(S)}}{\nu N_{Al}^{(0)}} \quad (9)$$

Where k_p is the rate constant, D_O is the oxidation diffusion coefficient, $N_O^{(S)}$ is the surface concentration, $N_{Al}^{(0)}$ is the original alloy concentration of *Al* element, ε is a constant reflecting diffusional blocking by Al_2O_3, and ν is the stoichiometric factor for the oxide particles $AlO_{1.5}$. According to Eqs. (8) and (9), the diffusion coefficient of oxidation (D_O) is the key determinant of *X*. Since the D_O is proportional to the exposure temperature [73], the depth of Al_2O_3 increased with the increasing exposure temperatures. In addition, Eqs. (8) and (9) indicated that the depth of Al_2O_3 particles gradually increased with longer exposure periods at a specific temperature, a trend confirmed by the results shown in Fig. 7 and 8.

In addition to the exposure temperature, the chemical composition of HEAs also determines the formation of Al_2O_3 particles. Our current results indicated that a duple-layer oxide film, including an outer layer of Cr_2O_3 and an inner layer of Al_2O_3, developed on $Al_{0.1}$CoCrFeNi HEA after 100 and 500 h of exposure, while a single layer of Cr_2O_3 formed after 1000 h of exposure, as displayed in Fig. 7-10. This result is a significant difference from the previous investigations on the oxidation behavior of Ni-Cr-Al alloys in high-temperature CO_2 or air environments. It is generally accepted that Ni-rich oxides would form in the outermost layer of the Ni-Cr-Al alloys after oxidation in these environments [38,77,78]. The main reason for the different microstructure of the oxide films is that the lower Ni concentration in $Al_{0.1}$CoCrFeNi HEA limited the formation of Ni-rich oxides. The Ni concentration in the current HEA is 22.95 ± 0.15 wt.%, while it is more than 50% in Ni-Cr-Al alloys. Besides, the chemical composition of the oxide films developed on $Al_{0.1}$CoCrFeNi HEA further suggested that only alloying elements, Cr and Al, were involved in forming the oxide films, as illustrated in Fig. 7. Al_2O_3 would develop on $Al_{0.1}$CoCrFeNi HEA at the initial stage of corrosion due to a lower Gibbs formation energy between Cr_2O_3 and Al_2O_3 [79]. However, a critical concentration of Al in HEA is needed to transition from internal oxidation to external oxidation. The critical concentration of Al to form external alumina scales can be

calculated based on Wagner's theory [80]. Since elements, such as Co and Fe, were not involved in forming oxide films, the calculation process was simplified to ternary Ni-Cr-Al alloy.

$$N_{Al}^{o*} = f_v^* \frac{F(h_{Al})}{\rho(AlO_{1.5})} \qquad (10)$$

Where $N_{Al}{}^{o*}$ is the critical concentration of Al to form external alumina scales, $\rho(AlO_{1.5})$ is the ratio of the molar volumes of the HEA and the oxide Al_2O_3, f_v^* is the critical value for the volume fraction of internal oxide, usually set equal to 0.3 [81], and h_{Al} is defined as [82]:

$$h_{Al} = \gamma\varphi_{Al} = \gamma \frac{D_O}{D_{Al}} \quad (11)$$

$$\varepsilon^2 = 4\gamma^2 D_O t \quad (12)$$

where D_O and D_{Al} are the diffusion coefficients for oxygen and Al in HEA [47,73], γ is a parameter related to the kinetics of internal oxidation, ε is the distance of the internal oxidation front from the original location of the alloy surface (6.71 ± 1.27 μm for 1000 h), and t is the time (3.6×10^6 s). $F(h_{Al})$ can be calculated by the following equation when an external scale of the oxides was existed [83]:

$$\frac{N_O^S(Cr)}{\nu_{N_{Al}^o} N_{Al}^O} = \frac{G(\gamma)}{F(h_{Al})} \frac{erf(\gamma) - erf(\mu_O)}{erf(\gamma)} \quad (13)$$

Where $N_o{}^S(Cr)$ is the oxygen concentration in the pure Cr at the oxygen pressure for the equilibrium between Cr and Cr_2O_3 [83]. μ_O can be calculated by the following equation [82]:

$$\mu_O = \frac{1}{2}\left(\frac{k_c(Cr_2O_3)}{D_O}\right)^{1/2} \quad (14)$$

$$G(\gamma) = \pi^{1/2}\gamma \exp(\gamma^2) erf(\gamma) \quad (15)$$

Where $k_c(Cr_2O_3)$ is the parabolic rate constant for the growth of Cr_2O_3 scales [83], $G(\gamma)$ is another auxiliary function. Substituting the previous data into the above equations yielded N_o (Al) = 13.79 at. %. This result suggested that Al concentration in the current $Al_{0.1}$CoCrFeNi HEA (2.43 at. %) was insufficient to form an outer Al_2O_3 layer. Furthermore, the minimum Al concentration required to form an external oxide layer should be more than 13.79 at. %. Previous investigations on the oxidation behavior of Al_xCoCrFeNi HEA in different high temperature environments further confirmed this conclusion [32,84]. For instance, S. Abbaszadeh *et al.* investigated the oxidation behavior of $Al_{0.5}$CoCrFeNi HEA (8.2 at. %) at different temperatures in air and reported the

formation of a Cr_2O_3 external and an Al_2O_3 internal oxide layer [32]. However, S. Wang *et al.* revealed that a continuous $(Al_{0.9}Cr_{0.1})_2O_3$ oxide film developed on the surface of $Al_{1.5}CoCrFeNiTi_{0.5}$ HEA (25 at. %) [84].

5. Conclusions

In this work, the corrosion behavior of an $Al_{0.1}CoCrFeNi$ HEA in high temperature CO_2 at 850 °C for 100, 500, and 1000 h was investigated. The microstructure evolution of oxide films was characterized using different equipment. The following conclusions can be drawn:

(1) Weight gain increased with exposure periods, following the parabolic law ($n=0.425$), but it was lower than that of 316LSS, nickel-based 601, and 617 alloys under similar corrosion conditions. These results suggested that the $Al_{0.1}CoCrFeNi$ HEA exhibited superior corrosion resistance compared to most conventional alloys in a high temperature CO_2 environment.

(2) Many irregular Cr_2O_3 particles were developed on the surface of the samples after 100 h of exposure. These oxide particles gradually aggregated and formed petal-shaped Cr_2O_3 oxides as the exposure period increased from 500 to 1000 h. These results indicated that the surface morphologies of the oxides on $Al_{0.1}CoCrFeNi$ HEA evolved with increased exposure periods, while their chemical composition remained stable.

(3) A double-layer oxide film structure, consisting of an outer Cr_2O_3 layer and an inner Al_2O_3 layer, developed on the samples after 100 and 500 h of exposure, while a single layer of Cr_2O_3 formed after 1000 h of exposure. The Cr_2O_3 film was composed of columnar grains rather than a dense oxide film, and the average size of these grains gradually increased with extended exposure periods. Besides, the thickness of the oxide films gradually increased as the exposure periods increased, measuring 0.66 ± 0.28 μm for 100 h, 0.98 ± 0.22 μm for 500 h, and 1.82 ± 0.14 μm for 1000 h, respectively. No significant carbon diffusion to the matrix was observed after different exposure periods.

(4) CoCrFeNi particles with an FCC structure were embedded in the oxide films regardless of the exposure period, possibly due to grain boundary sliding while relieving the compressive stress. Besides, a transition zone containing a large number of striped-like Al_2O_3 oxides was formed underneath the Cr_2O_3 oxide films after different exposure periods. Furthermore, the thickness of the transition zone gradually increased with prolonged exposure periods.

Acknowledgments

This work was financially supported by the National Natural Science Foundation of China (12105044), Jiangxi Provincial Natural Science (20202BABL211014), Foundation of Jiangxi Educational Committee (GJJ180401), and Doctoral Scientific Research Foundation of East China University of Technology (DHBK2017127).

References

[1] I. Hanif, Impact of fossil fuels energy consumption, energy policies, and urban sprawl on carbon emissions in East Asia and the Pacific: A panel investigation, Energy Strateg. Rev. 21 (2018) 16–24, https://doi.org/10.1016/j.esr.2018.04.006.

[2] J.B. Sun, C. Sun, G.A. Zhang, X.D. Li, W.M. Zhao, T. Jiang, H.F. Liu, X.K. Cheng, Y. Wang, Effect of O_2 and H_2S impurities on the corrosion behavior of X65 steel in water-saturated supercritical CO_2 system, Corros. Sci. 107 (2016) 31–40, https://doi.org/10.1016/j.corsci.2016.02.017.

[3] Y.-S. Choi, S. Nešić, Determining the corrosive potential of CO_2 transport pipeline in high pCO_2–water environments, Int. J. Greenh. Gas Control 5 (2011) 788–797, https://doi.org/10.1016/j.ijggc.2010.11.008.

[4] Y. Xie, J.Q. Zhang, D.J. Young, Temperature Effect on Oxidation Behavior of Ni-Cr Alloys in CO_2 Gas Atmosphere, J. Electrochem. Soc. 164 (2017) C285–C293, https://doi.org/10.1149/2.1021706jes.

[5] P. Tafur-Escanta, I. López-Paniagua, J. Muñoz-Antón, Thermodynamics analysis of the supercritical CO_2 binary mixtures for Brayton power cycles, Energy 270 (2023) 126838, https://doi.org/10.1016/j.energy.2023.126838.

[6] M.T. White, G. Bianchi, L. Chai, S.A. Tassou, A.I. Sayma, Review of supercritical CO_2 technologies and systems for power generation, Appl. Therm. Eng. 185 (2021) 116447, https://doi.org/10.1016/j.applthermaleng.2020.116447.

[7] R.P. Oleksak, J.P. Baltrus, J. Nakano, A. Nakano, G.R. Holcomb, Ö.N. Doğan, Mechanistic insights into the oxidation behavior of Ni alloys in high-temperature CO_2, Corros. Sci. 125 (2017) 77–86, https://doi.org/10.1016/j.corsci.2017.06.005.

[8] R.P. Oleksak, J.H. Tylczak, G.R. Holcomb, Ö.N. Doğan, High temperature oxidation of steels in CO_2 containing impurities, Corros. Sci. 164 (2020) 108316, https://doi.org/10.1016/j.corsci.2019.108316.

[9] H.J. Lee, G.O. Subramanian, S.H. Kim, C.H. Jang, Effect of pressure on the corrosion and carburization behavior of chromia-forming heat-resistant alloys in high-temperature carbon dioxide environments, Corros. Sci. 111 (2016) 649–658, https://doi.org/10.1016/j.corsci.2016.06.004.

[10] F. Rouillard, T. Furukawa, Corrosion of 9-12Cr ferritic–martensitic steels in high-temperature CO_2, Corros. Sci. 105 (2016) 120–132, https://doi.org/10.1016/j.corsci.2016.01.009.

[11] Z.L. Zhu, Y. Cheng, B. Xiao, H.I. Khan, H. Xu, N.Q. Zhang, Corrosion behavior of ferritic and ferritic-martensitic steels in supercritical carbon dioxide, Energy 175 (2019) 1075–1084, https://doi.org/10.1016/j.energy.2019.03.146.

[12] A. Brittan, J. Mahaffey, M. Anderson, Corrosion and Mechanical Performance of Grade 92 Ferritic-Martensitic Steel After Exposure to Supercritical Carbon Dioxide, Metall. Mater. Trans. A 51 (2020) 2564–2572, https://doi.org/10.1007/s11661-020-05691-7.

[13] G. Cao, V. Firouzdor, K. Sridharan, M. Anderson, T.R. Allen, Corrosion of austenitic alloys in high temperature supercritical carbon dioxide, Corros. Sci. 60 (2012) 246–255, https://doi.org/10.1016/j.corsci.2012.03.029.

[14] T.D. Nguyen, J.Q. Zhang, D.J. Young, Effects of cerium and manganese on corrosion of Fe–Cr and Fe–Cr–Ni alloys in Ar–20CO_2 gas at 818 °C, Corros. Sci. 76 (2013) 231–242, https://doi.org/10.1016/j.corsci.2013.06.046.

[15] T. Gheno, D. Monceau, J.Q. Zhang, D.J. Young, Carburisation of ferritic Fe–Cr alloys by low carbon activity gases, Corros. Sci. 53 (2011) 2767–2777, https://doi.org/10.1016/j.corsci.2011.05.013.

[16] Z.M. Li, D. Raabe, Strong and Ductile Non-equiatomic High-Entropy Alloys: Design, Processing, Microstructure, and Mechanical Properties, JOM 69 (2017) 2099–2106, https://doi.org/10.1007/s11837-017-2540-2.

[17] Z.M. Li, K.G. Pradeep, Y. Deng, D. Raabe, C.C. Tasan, Metastable high-entropy dual-phase alloys overcome the strength–ductility trade-off, Nature 534 (2016) 227–230, https://doi.org/10.1038/nature17981.

[18] M.-G. Jo, J.-Y. Suh, M.-Y. Kim, H.-J. Kim, W.-S. Jung, D.-I. Kim, H.N. Han, High temperature tensile and creep properties of CrMnFeCoNi and CrFeCoNi high-entropy

alloys, Mater. Sci. Eng. A 838 (2022) 142748, https://doi.org/10.1016/j.msea.2022.142748.

[19] Y. Fu, J. Li, H. Luo, C.W. Du, X.G. Li, Recent advances on environmental corrosion behavior and mechanism of high-entropy alloys, J. Mater. Sci. Technol. 80 (2021) 217–233, https://doi.org/10.1016/j.jmst.2020.11.044.

[20] J.W. Yeh, Y.L. Chen, S.J. Lin, S.K. Chen, High-Entropy Alloys – A New Era of Exploitation, Mater. Sci. Forum 560 (2007) 1–9, https://doi.org/10.4028/www.scientific.net/MSF.560.1.

[21] A.I. Thorhallsson, I. Csáki, L.E. Geambazu, F. Magnus, S.N. Karlsdottir, Effect of alloying ratios and Cu-addition on corrosion behaviour of CoCrFeNiMo high-entropy alloys in superheated steam containing CO_2, H_2S and HCl, Corros. Sci. 178 (2021) 109083, https://doi.org/10.1016/j.corsci.2020.109083.

[22] W. Kai, F.C. Chien, F.P. Cheng, R.T. Huang, J.J. Kai, C.T. Liu, The corrosion of an equimolar FeCoNiCrMn high-entropy alloy in various CO_2/CO mixed gases at 700 and 950 °C, Corros. Sci. 153 (2019) 150–161, https://doi.org/10.1016/j.corsci.2019.03.030.

[23] F.J. Wang, Y. Zhang, G.L. Chen, H.A. Davies, Cooling Rate and Size Effect on the Microstructure and Mechanical Properties of AlCoCrFeNi High Entropy Alloy, J. Eng. Mater. Technol. 131 (2009), https://doi.org/10.1115/1.3120387.

[24] H.-P. Chou, Y.-S. Chang, S.-K. Chen, J.-W. Yeh, Microstructure, thermophysical and electrical properties in $Al_xCoCrFeNi$ ($0 \leq x \leq 2$) high-entropy alloys, Mater. Sci. Eng. B 163 (2009) 184–189, https://doi.org/10.1016/j.mseb.2009.05.024.

[25] M. Tokarewicz, M. Grądzka-Dahlke, Review of Recent Research on AlCoCrFeNi High-Entropy Alloy, Metals (Basel). 11 (2021) 1302, https://doi.org/10.3390/met11081302.

[26] W.-R. Wang, W.-L. Wang, S.-C. Wang, Y.-C. Tsai, C.-H. Lai, J.-W. Yeh, Effects of Al addition on the microstructure and mechanical property of $Al_xCoCrFeNi$ high-entropy alloys, Intermetallics 26 (2012) 44–51, https://doi.org/10.1016/j.intermet.2012.03.005.

[27] T.F. Yang, S.Q. Xia, S. Liu, C.X. Wang, S.S. Liu, Y. Zhang, J.M. Xue, S. Yan, Y.G. Wang, Effects of Al addition on microstructure and mechanical properties of $Al_xCoCrFeNi$ High-entropy alloy, Mater. Sci. Eng. A 648 (2015) 15–22, https://doi.org/10.1016/j.msea.2015.09.034.

[28] Q. Chao, J. Joseph, M. Annasamy, P. Hodgson, M.R. Barnett, D. Fabijanic, $Al_xCoCrFeNi$ high entropy alloys from metal scrap: Microstructure and mechanical properties, J. Alloys Compd. 976 (2024) 173002, https://doi.org/10.1016/j.jallcom.2023.173002.

[29] T.M. Butler, M.L. Weaver, Oxidation behavior of arc melted AlCoCrFeNi multi-component high-entropy alloys, J. Alloys Compd. 674 (2016) 229–244, https://doi.org/10.1016/j.jallcom.2016.02.257.

[30] B. Yin, X.S. Guo, D. Zhang, X.Y. San, Influence of multiphase evolution on corrosion resistance of $Al_xCoCrFeNi$ alloys determined by transmission electron microscopy, J. Alloys Compd. 947 (2023) 169534, https://doi.org/10.1016/j.jallcom.2023.169534.

[31] Y.Y. Liu, Z. Chen, Y.Z. Chen, J.C. Shi, Z.Y. Wang, S. Wang, F. Liu, Effect of Al content on high temperature oxidation resistance of $Al_xCoCrCuFeNi$ high entropy alloys (x=0, 0.5, 1, 1.5, 2), Vacuum 169 (2019) 108837, https://doi.org/10.1016/j.vacuum.2019.108837.

[32] S. Abbaszadeh, A. Pakseresht, H. Omidvar, A. Shafiei, Investigation of the High-Temperature Oxidation Behavior of the $Al_{0.5}CoCrFeNi$ High Entropy Alloy, Surfaces and Interfaces 21 (2020) 100724, https://doi.org/10.1016/j.surfin.2020.100724.

[33] K. Li, W. Chen, Recent progress in high-entropy alloys for catalysts: synthesis, applications, and prospects, Mater. Today Energy 20 (2021) 100638, https://doi.org/10.1016/j.mtener.2021.100638.

[34] S.W. Wu, G. Wang, J. Yi, Y.D. Jia, I. Hussain, Q.J. Zhai, P.K. Liaw, Strong grain-size effect on deformation twinning of an $Al_{0.1}CoCrFeNi$ high-entropy alloy, Mater. Res. Lett. 5 (2017) 276–283. https://doi.org/10.1080/21663831.2016.1257514.

[35] Y.L. Bian, Z.D. Feng, N.B. Zhang, Y.X. Li, X.F. Wang, B.B. Zhang, Y. Cai, L. Lu, S. Chen, X.H. Yao, S.N. Luo, Ultrafast severe plastic deformation in high-entropy alloy $Al_{0.1}CoCrFeNi$ via dynamic equal channel angular pressing, Mater. Sci. Eng. A 847 (2022) 143221, https://doi.org/10.1016/j.msea.2022.143221.

[36] Y.H. Li, S.Z. Wang, P.P. Sun, Z.X. Tong, D.H. Xu, Y. Guo, J.Q. Yang, Early oxidation of Super304H stainless steel and its scales stability in supercritical water environments, Int. J. Hydrogen Energy 41 (2016) 15764–15771, https://doi.org/10.1016/j.ijhydene.2016.04.144.

[37] J.J. Shen, L.J. Zhou, T.F. Li, High-temperature oxidation of Fe-Cr alloys in wet oxygen, Oxid. Met. 48 (1997) 347–356, https://doi.org/10.1007/BF01670507.

[38] H.Y. Li, T.D. Nguyen, J.Q. Zhang, Corrosion Behaviour of Ni-based Alloys 230, 617 and 601 in CO_2 Gas at 750 and 850 °C, J. Electrochem. Soc. 171 (2024) 031502, https://doi.org/10.1149/1945-7111/ad2db3.

[39] L.T. Wang, D. Mercier, S. Zanna, A. Seyeux, M. Laurent-Brocq, L. Perrière, I. Guillot, P. Marcus, Study of the surface oxides and corrosion behaviour of an equiatomic CoCrFeMnNi high entropy alloy by XPS and ToF-SIMS, Corros. Sci. 167 (2020) 108507, https://doi.org/10.1016/j.corsci.2020.108507.

[40] E. Gardin, S. Zanna, A. Seyeux, A. Allion-Maurer, P. Marcus, Comparative study of the surface oxide films on lean duplex and corresponding single phase stainless steels by XPS and ToF-SIMS, Corros. Sci. 143 (2018) 403–413, https://doi.org/10.1016/j.corsci.2018.08.009.

[41] X.L. Guo, Z. Liu, L. Li, J.C. Cheng, H.Z. Su, L.F. Zhang, Revealing the long-term oxidation and carburization mechanism of 310S SS and Alloy 800H exposed to supercritical carbon dioxide, Mater. Charact. 183 (2022) 111603, https://doi.org/10.1016/j.matchar.2021.111603.

[42] F.S. Pettit, J.B. Wagner, Oxidation of cobalt in CO-CO_2 mixtures in the temperature range 920°C–1200 °C, Acta Metall. 12 (1964) 41–47, https://doi.org/10.1016/0001-6160(64)90052-5.

[43] A. Roine, HSC Chemistry 6.0, Outokumpu Research Oy, Pori, Finland, 2006.

[44] L.J. Yang, H.C. Qian, W.J. Kuang, Corrosion Behaviors of Heat-Resisting Alloys in High Temperature Carbon Dioxide, Materials (Basel). 15 (2022) 1331, https://doi.org/10.3390/ma15041331.

[45] R.P. Oleksak, J.H. Tylczak, Ö.N. Doğan, High-Temperature Oxidation of Steels in Direct-Fired CO_2 Power Cycle Environments, JOM 73 (2021) 3965–3973, https://doi.org/10.1007/s11837-021-04960-z.

[46] R.I. Olivares, W. Stein, T.D. Nguyen, D.J. Young, Corrosion of Nickel-Base Alloys by Supercritical CO_2, Advances in Materials Technology for Fossil Power Plants-Proceedings from the 8th International Coference, 2016, 888–899, https://doi.org/10.31399/asm.cp.am-epri-2016p0888.

[47] A. Mehta, Y. Sohn, Investigation of sluggish diffusion in FCC $Al_{0.25}CoCrFeNi$ high-entropy alloy, Mater. Res. Lett. 9 (2021) 239–246, https://doi.org/10.1080/21663831.2021.1878475.

[48] J.P. Gibbs, Corrosion of various engineering alloys in supercritical carbon dioxide, Massachusetts Institute of Technology, 2010, http://hdl.handle.net/1721.1/59247.

[49] G. Zhang, Y.-P. Huang, E. Jiang, W.-W. Liu, H. Yang, J. Xiong, Y.-F. Zhao, Effect of aluminium addition on the oxidation and carburization behaviour of austenitic stainless in high-temperature SCO_2 environments, Corros. Sci. 226 (2024) 111666, https://doi.org/10.1016/j.corsci.2023.111666.

[50] H.S. Chen, J.D. Luo, T.F. Zhang, C.H. Jang, R. Tang, B.J. Dong, J. Li, X.S. Leng, Microstructures, tensile properties and corrosion behaviors of $Fe_{20}Cr_{25}NiNb$ stainless steels with different Al contents in supercritical carbon dioxide, J. Mater. Res. Technol. 23 (2023) 5246–5259, https://doi.org/10.1016/j.jmrt.2023.02.224.

[51] G. Costa, A. Garg, M.P. Brady, Corrosion of alumina-forming austenitic alloys under the supercritical carbon dioxide-based venus atmospheric surface conditions, Corros. Sci. 211 (2023) 110882, https://doi.org/10.1016/j.corsci.2022.110882.

[52] G. O. Subramanian, S.H. Kim, J.J. Chen, C.H. Jang, Supercritical-CO_2 corrosion behavior of alumina- and chromia-forming heat resistant alloys with Ti, Corros. Sci. 188 (2021) 109531, https://doi.org/10.1016/j.corsci.2021.109531.

[53] Z. Liu, Q.Y. Zhou, S. Cong, Z.G. Duan, Z.D.D. Ma, M. Shu, Z.J. Zhou, L.F. Zhang, X.L. Guo, Corrosion behavior of a new alumina-forming duplex stainless steel with different surface treatment in supercritical carbon dioxide, Surf. Coatings Technol. 466 (2023) 129619, https://doi.org/10.1016/j.surfcoat.2023.129619.

[54] J.-W. Yeh, Alloy Design Strategies and Future Trends in High-Entropy Alloys, JOM 65 (2013) 1759–1771, https://doi.org/10.1007/s11837-013-0761-6.

[55] E.P. George, D. Raabe, R.O. Ritchie, High-entropy alloys, Nat. Rev. Mater. 4 (2019) 515–534, https://doi.org/10.1038/s41578-019-0121-4.

[56] F.H. Stott, G.C. Wood, Internal oxidation, Mater. Sci. Technol. 4 (1988) 1072–1078, https://doi.org/10.1179/mst.1988.4.12.1072.

[57] F.H. Stott, Y. Shida, D.P. Whittle, G.C. Wood, B.D. Bastow, The morphological and structural development of internal oxides in nickel-aluminum alloys at high temperatures, Oxid. Met. 18 (1982) 127–146, https://doi.org/10.1007/BF00662034.

[58] C.H. Xu, W. Gao, Pilling-Bedworth ratio for oxidation of alloys, Mater. Res. Innov. 3 (2000) 231–235, https://doi.org/10.1007/s100190050008.

[59] V. Sorkin, Z.G. Yu, S. Chen, T.L. Tan, Z. Aitken, Y.-W. Zhang, First principles-based design of lightweight high entropy alloys, Sci. Rep. 13 (2023) 22549, https://doi.org/10.1038/s41598-023-49258-z.

[60] M.B. Pilling, R.E. Bedworth, The oxidation of metals at high temperatures, Inst Met. 29 (1923) 529.

[61] Y. Shida, F.H. Stott, B.D. Bastow, D.P. Whittle, G.C. Wood, Development of preferential intergranular oxides in nickel-aluminum alloys at high temperatures, Oxid. Met. 18 (1982) 93–113, https://doi.org/10.1007/BF00662032.

[62] J.A. Nychka, C. Pullen, D.R. Clarke, Surface oxide cracking associated with oxidation-induced grain boundary sliding in the underlying alloy, Acta Mater. 52 (2004) 1097–1105, https://doi.org/10.1016/j.actamat.2003.10.042.

[63] G.C. Wood, F.H. Stott, D.P. Whittle, Y. Shida, B.D. Bastow, The high-temperature internal oxidation and intergranular oxidation of nickel-chromium alloys, Corros. Sci. 23 (1983) 9–25, https://doi.org/10.1016/0010-938X(83)90056-2.

[64] J.R. Mackert, R.D. Ringle, C.W. Fairhurst, High-temperature Behavior of a Pd-Ag Alloy for Porcelain, J. Dent. Res. 62 (1983) 1229–1235, https://doi.org/10.1177/00220345830620121201.

[65] T.L. Barth, E.A. Marquis, The Effect of Ti on the Early Stages of Oxidation of an Alumina-Forming NiCrAl Alloy, Oxid. Met. 92 (2019) 13–26, https://doi.org/10.1007/s11085-019-09911-3.

[66] S. Guruswamy, S.M. Park, J.P. Hirth, R.A. Rapp, Internal oxidation of Ag-in alloys: Stress relief and the influence of imposed strain, Oxid. Met. 26 (1986) 77–100, https://doi.org/10.1007/BF00664274.

[67] M.M. Nagl, W.T. Evans, The mechanical failure of oxide scales under tensile or compressive load, J. Mater. Sci. 28 (1993) 6247–6260, https://doi.org/10.1007/BF01352181.

[68] P. Sarobol, J.E. Blendell, C.A. Handwerker, Whisker and hillock growth via coupled localized Coble creep, grain boundary sliding, and shear induced grain boundary migration, Acta Mater. 61 (2013) 1991–2003, https://doi.org/10.1016/j.actamat.2012.12.019.

[69] H.E. Evans, Stress effects in high temperature oxidation of metals, Int. Mater. Rev. 40 (1995) 1–40, https://doi.org/10.1179/imr.1995.40.1.1.

[70] J. Lu, G.L. Ren, Y. Chen, H. Zhang, L. Li, A.H. Huang, X.Z. Liu, H.Y. Cai, X. Shan, L.R. Luo, X.C. Zhang, X.F. Zhao, Unraveling the oxidation mechanism of an AlCoCrFeNi high-entropy alloy at 1100 °C, Corros. Sci. 209 (2022) 110736, https://doi.org/10.1016/j.corsci.2022.110736.

[71] L.-F. He, P. Roman, B. Leng, K. Sridharan, M. Anderson, T.R. Allen, Corrosion behavior of an alumina forming austenitic steel exposed to supercritical carbon dioxide, Corros. Sci. 82 (2014) 67–76, https://doi.org/10.1016/j.corsci.2013.12.023.

[72] L. Tan, M. Anderson, D. Taylor, T.R. Allen, Corrosion of austenitic and ferritic-martensitic steels exposed to supercritical carbon dioxide, Corros. Sci. 53 (2011) 3273–3280, https://doi.org/10.1016/j.corsci.2011.06.002.

[73] D.P. Whittle, Y. Shida, G.C. Wood, F.H. Stott, B.D. Bastow, Enhanced diffusion of oxygen during internal oxidation of nickel-base alloys, Philos. Mag. A 46 (1982) 931–949, https://doi.org/10.1080/01418618208236942.

[74] Y.H. Kim, H. Jeong, B.-R. Won, H.J. Jeon, C.H. Park, D. Park, Y. Kim, S. Lee, J.H. Myung, Nanoparticle Exsolution on Perovskite Oxides: Insights into Mechanism, Characteristics and Novel Strategies, Nano-Micro Lett. 16 (2024) 33, https://doi.org/10.1007/s40820-023-01258-4.

[75] D.J. Young, M.L. Burg, P.R. Munroe, Internal Precipitation of Al_2O_3 and Cr_2O_3 in Austenitic Alloys, Mater. Sci. Forum 461–464 (2004) 21–28, https://doi.org/10.4028/www.scientific.net/MSF.461-464.21.

[76] S. Han, D.J. Young, Simultaneous internal oxidation and nitridation of Ni-Cr-Al alloys, Oxid. Met. 55 (2001) 223–242, https://doi.org/10.1023/a:1010304026026.

[77] T.J. Nijdam, L.P.H. Jeurgens, W.G. Sloof, Effect of partial oxygen pressure on the initial stages of high-temperature oxidation of γ-NiCrAl alloys, Mater. High Temp. 20 (2003) 311–318, https://doi.org/10.1179/mht.2003.037.

[78] T.J. Nijdam, L.P.H. Jeurgens, W.G. Sloof, Promoting exclusive α-Al_2O_3 growth upon high-temperature oxidation of NiCrAl alloys: experiment versus model predictions, Acta Mater. 53 (2005) 1643–1653, https://doi.org/10.1016/j.actamat.2004.12.014.

[79] H. Lu, C.L. Bao, D.H. Shen, J. Qin, Y.X. Cui, Y.X. Wang, STUDIES OF Cr/Al_2O_3 INTERFACIAL REACTIONS, J. Phys. Chem. Solids 58 (1997) 257–270, https://doi.org/10.1016/S0022-3697(96)00127-8.

[80] C. Wagner, Reaktionstypen bei der Oxydation von Legierungen, Zeitschrift Für Elektrochemie, Berichte Der Bunsengesellschaft Für Phys. Chemie 63 (1959) 772–782, https://doi.org/10.1002/bbpc.19590630713.

[81] R.A. Rapp, Kinetics, Microstructures and Mechanism of Internal Oxidation - Its Effect and Prevention in High Temperature Alloy Oxidation, Corros. 21 (1965) 382–401, https://doi.org/10.5006/0010-9312-21.12.382.

[82] Y. Niu, X.J. Zhang, Y. Wu, F. Gesmundo, The third-element effect in the oxidation of Ni–*x*Cr–7Al (*x*=0, 5, 10, 15at.%) alloys in 1atm O_2 at 900–1000 °C, Corros. Sci. 48 (2006) 4020–4036, https://doi.org/10.1016/j.corsci.2006.03.008.

[83] Y. Niu, F. Gesmundo, The Internal Oxidation of Ternary Alloys. V: The Transition from Internal to External Oxidation of the Most-Reactive Component under Low Oxidant Pressures, Oxid. Met. 62 (2004) 391–410, https://doi.org/10.1007/s11085-004-0919-2.

[84] S. Wang, Z. Chen, P. Zhang, K. Zhang, C.L. Chen, B.L. Shen, Influence of Al content on high temperature oxidation behavior of Al_xCoCrFeNiTi0.5 high entropy alloys, Vacuum 163 (2019) 263–268, https://doi.org/10.1016/j.vacuum.2019.01.053.

Figure captions

Fig. 1 Schematic diagram of high-temperature CO_2 corrosion test facility.

Fig. 2 The initial microstructure of $Al_{0.1}CoCrFeNi$ HEA: (a) XRD pattern and (b) EBSD image.

Fig. 3 SEM-EDS mapping images of the as-cast $Al_{0.1}CoCrFeNi$ HEA.

Fig. 4 Weight gain as a function of exposure time for different alloys in high temperature CO_2 at 850 ℃ [38].

Fig. 5 XRD patterns of $Al_{0.1}CoCrFeNi$ HEA corroded in a high temperature CO_2 environment at 850 ℃ for different exposure times.

Fig. 6 Low and high magnification SEM images of $Al_{0.1}CoCrFeNi$ HEA after being exposed to high-temperature CO_2 at 850 °C for different testing periods: (a) and (d) 100 h, (b) and (e) 500 h, (c) and (f) 1000 h.

Fig. 7 Cross-sectional SEM images and the results of EDS mapping and line analysis of the $Al_{0.1}CoCrFeNi$ HEA after exposure to high temperature CO_2 for different periods: (a) 100 h, (b) 500 h, and (c) 1000 h.

Fig. 8 ToF-SIMS depth profiles obtained on the $Al_{0.1}CoCrFeNi$ HEA after exposure to high temperature CO_2 for different periods: (a) 100 h, (b) 500 h, and (c) 1000 h.

Fig. 9 TEM analysis of the cross-section of the oxide film developed on $Al_{0.1}CoCrFeNi$ HEA after 100 h of exposure at 850 ℃ CO_2: (a) TEM image and corresponding EDS mapping, (b) the elemental EDS line (Line 4) scanning map of the oxide layer marked in the image (a); (c) TEM image and corresponding FFT pattern of the outer oxide layer; (d) high-resolution image and corresponding FFT pattern marked in the image (a); (e) and (f) SAED patterns of the positions marked in the image (a).

Fig. 10 TEM analysis of the cross-section of the oxide film developed on $Al_{0.1}CoCrFeNi$ HEA after 1000 h of exposure at 850 ℃ CO_2: (a) TEM image and corresponding EDS mapping, (b) the elemental EDS line (Line 5) scanning map of the oxide layer marked in the image (a); (c) TEM image and FFT pattern of the outer oxide layer; (d) high-resolution image and corresponding FFT pattern marked in the image (a); (e) and (f) SAED patterns of the positions marked in the image (a).

Fig. 11 Al concentrations in $Al_{0.1}CoCrFeNi$ HEA and oxide film after 100 h of exposure at different positions.

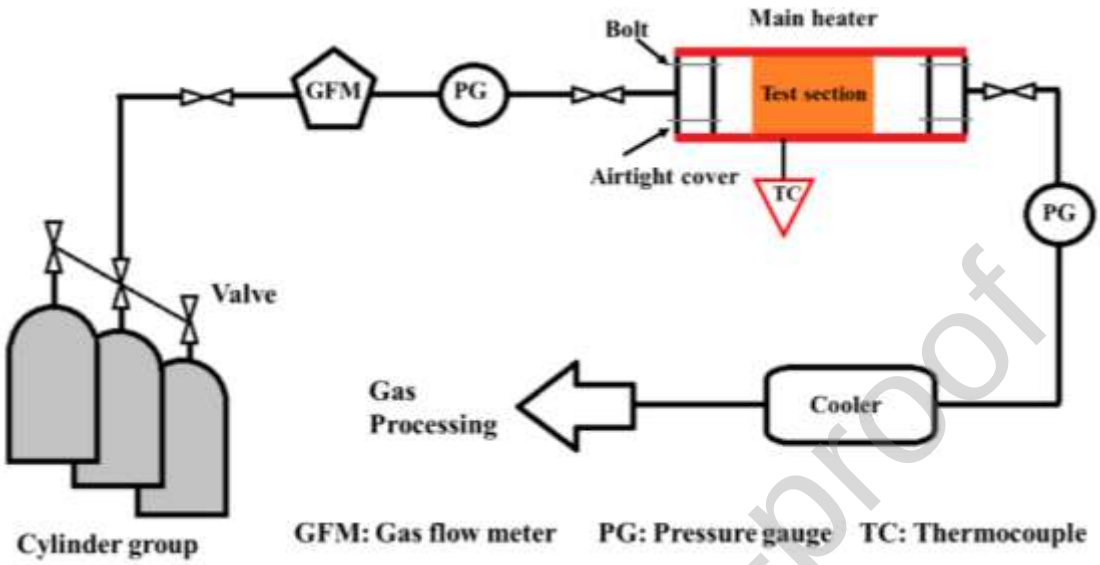

Figure 1 Schematic diagram of high-temperature CO_2 corrosion test facility.

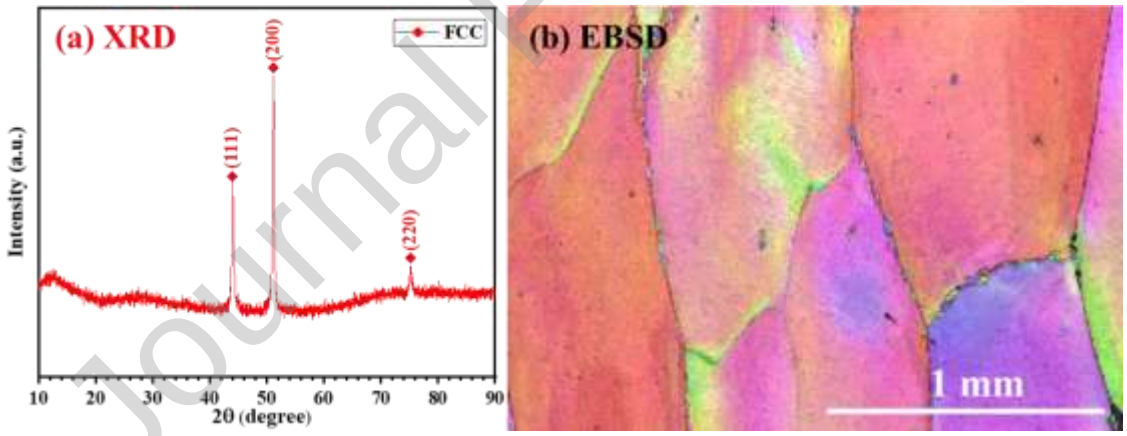

Figure 2 The initial microstructure of $Al_{0.1}CoCrFeNi$ HEA: (a) XRD pattern and (b) EBSD image.

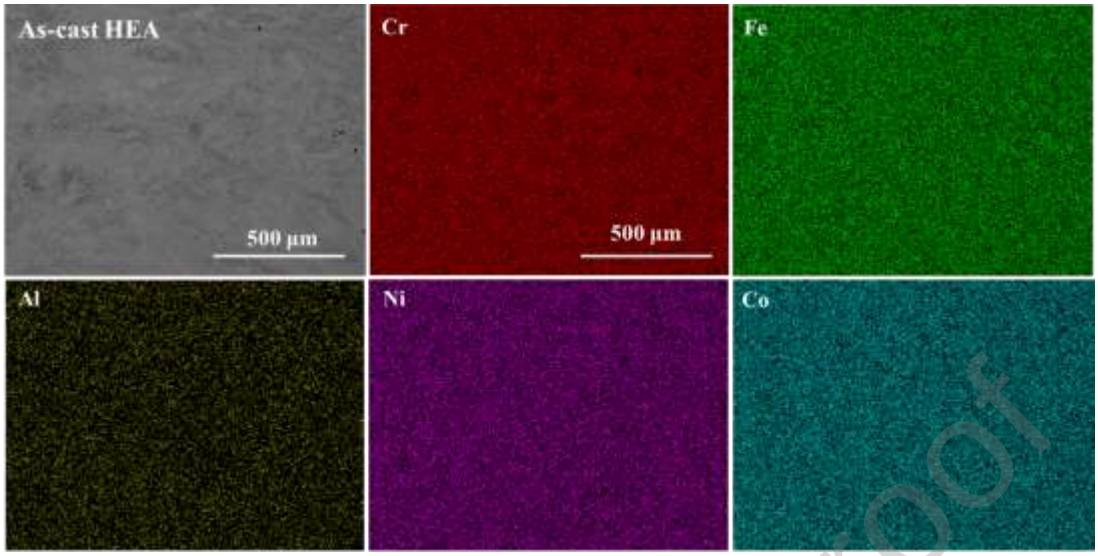

Figure 3 SEM-EDS mapping images of the as-cast $Al_{0.1}CoCrFeNi$ HEA.

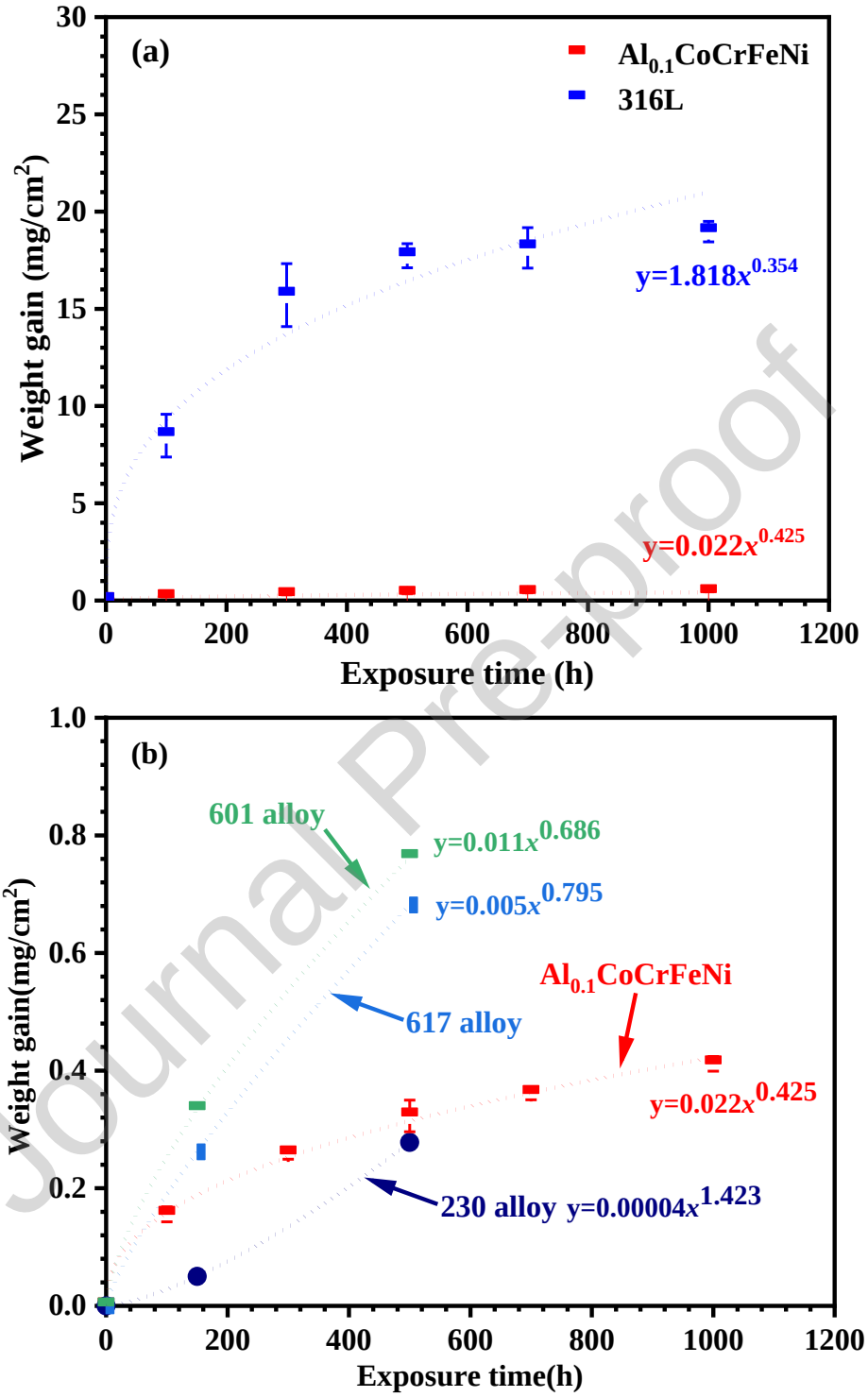

Figure 4 Weight gain as a function of exposure time for different alloys in high temperature CO_2 at 850 ℃ [38].

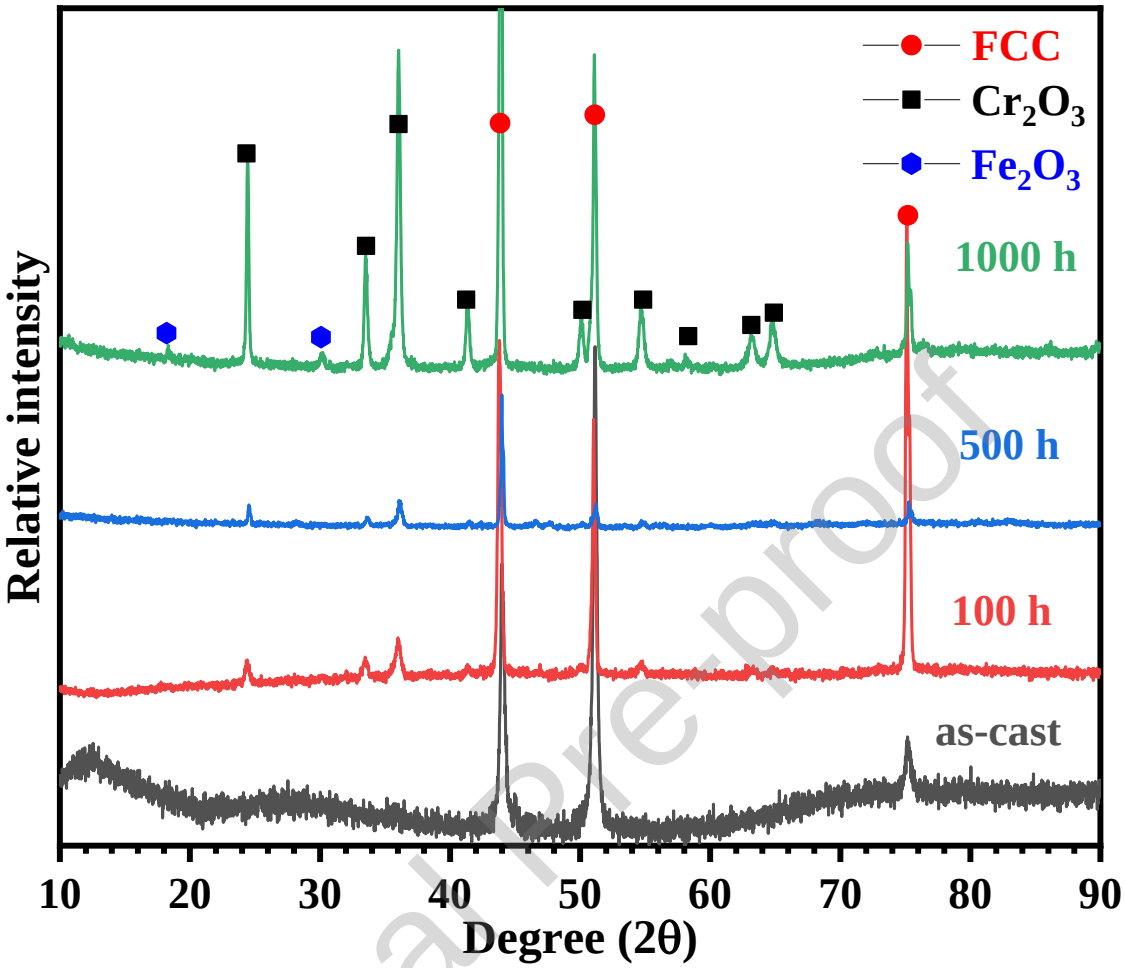

Figure 5 XRD patterns of $Al_{0.1}CoCrFeNi$ HEA corroded in high temperature CO_2 at 850 ℃ for different exposure times.

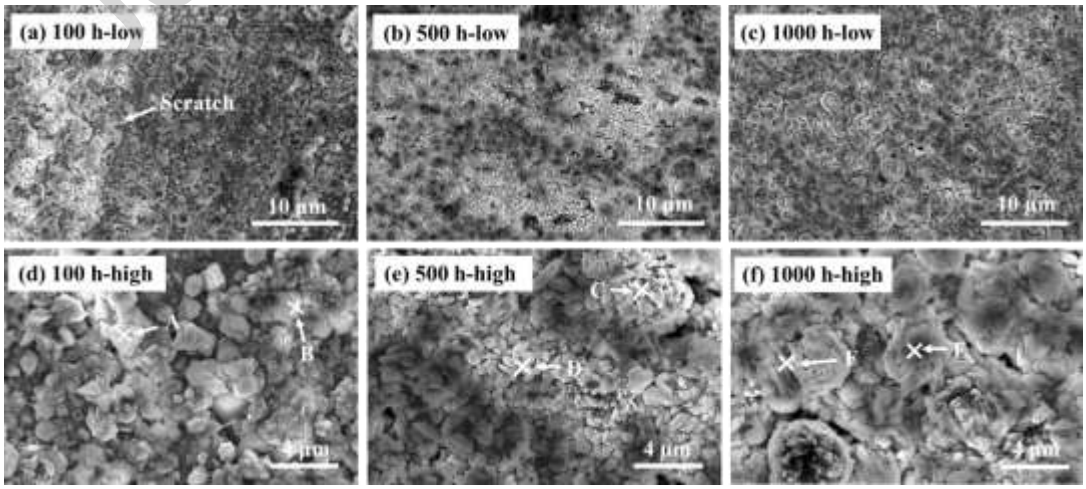

Figure 6 Low and high magnification SEM images of $Al_{0.1}CoCrFeNi$ HEA after being exposed to high-temperature CO_2 at 850 °C for different testing periods: (a) and (d) 100 h, (b) and (e) 500 h, (c) and (f) 1000 h.

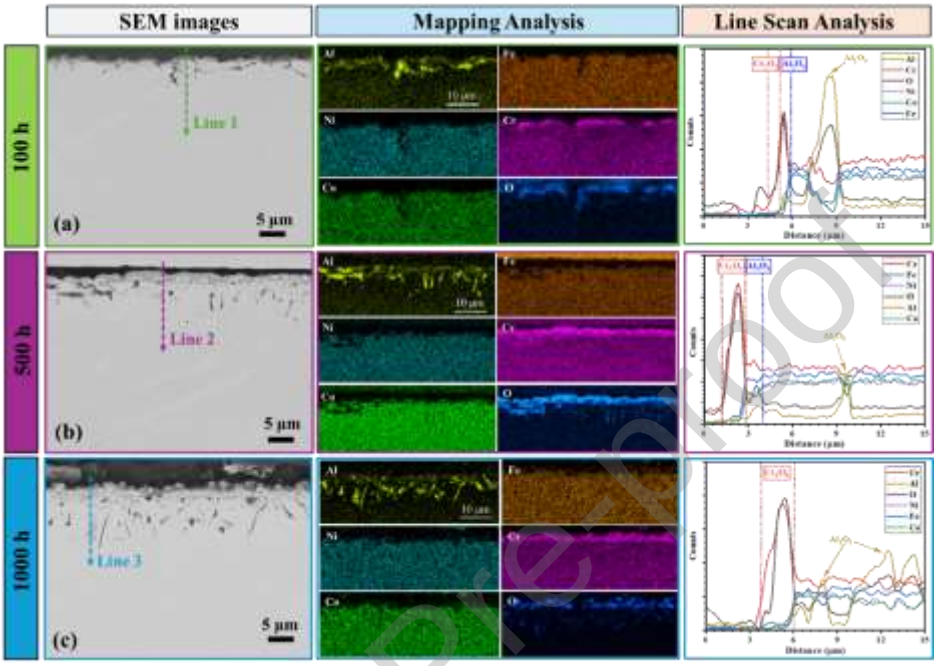

Figure 7 Cross-sectional SEM images and the results of EDS mapping and line analysis of the $Al_{0.1}CoCrFeNi$ HEA after exposure to high temperature CO_2 for different periods: (a) 100 h, (b) 500 h, and (c) 1000 h.

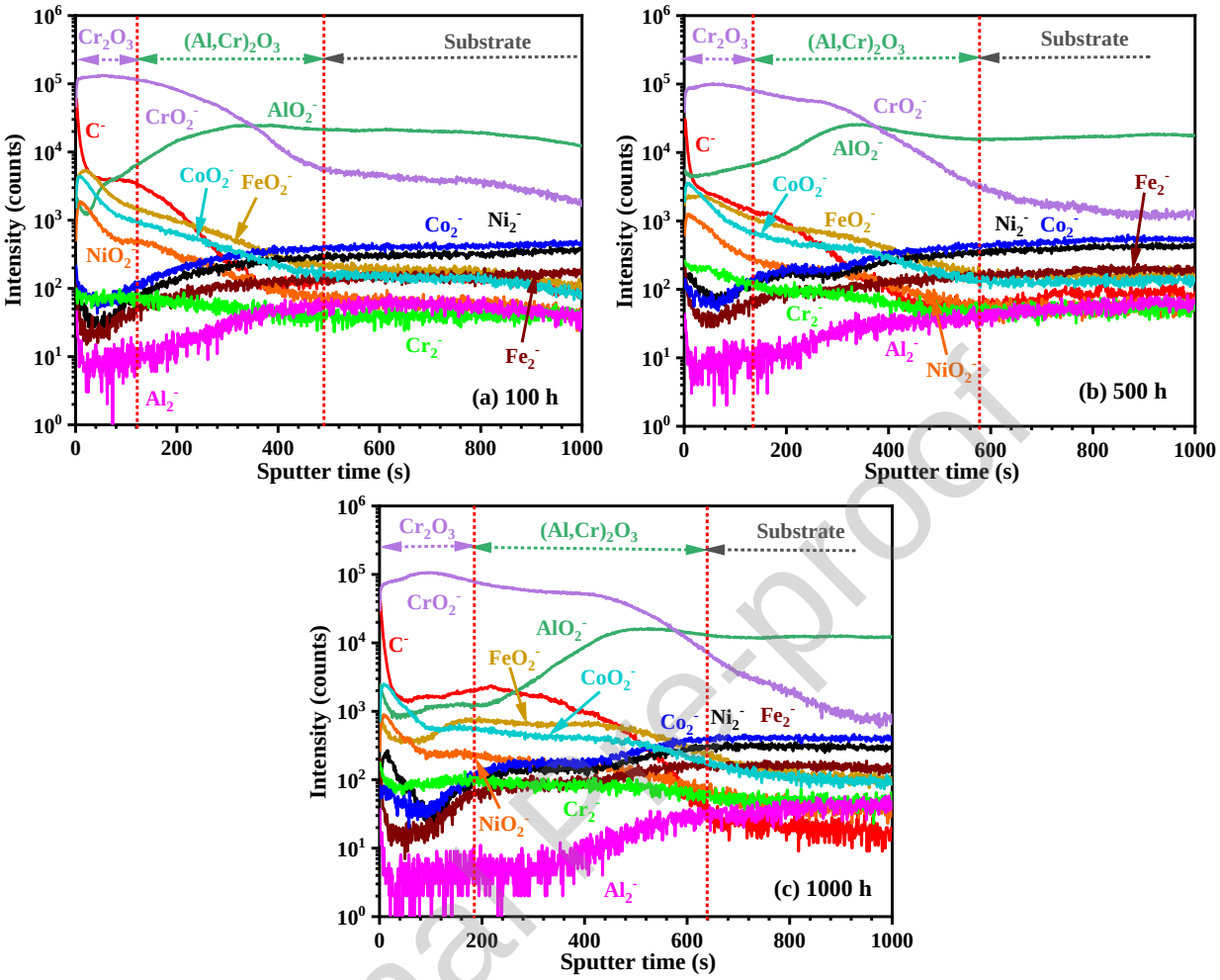

Figure 8 ToF-SIMS depth profiles obtained on the $Al_{0.1}CoCrFeNi$ HEA after exposure to high temperature CO_2 for different periods: (a) 100 h, (b) 500 h, and (c) 1000 h.

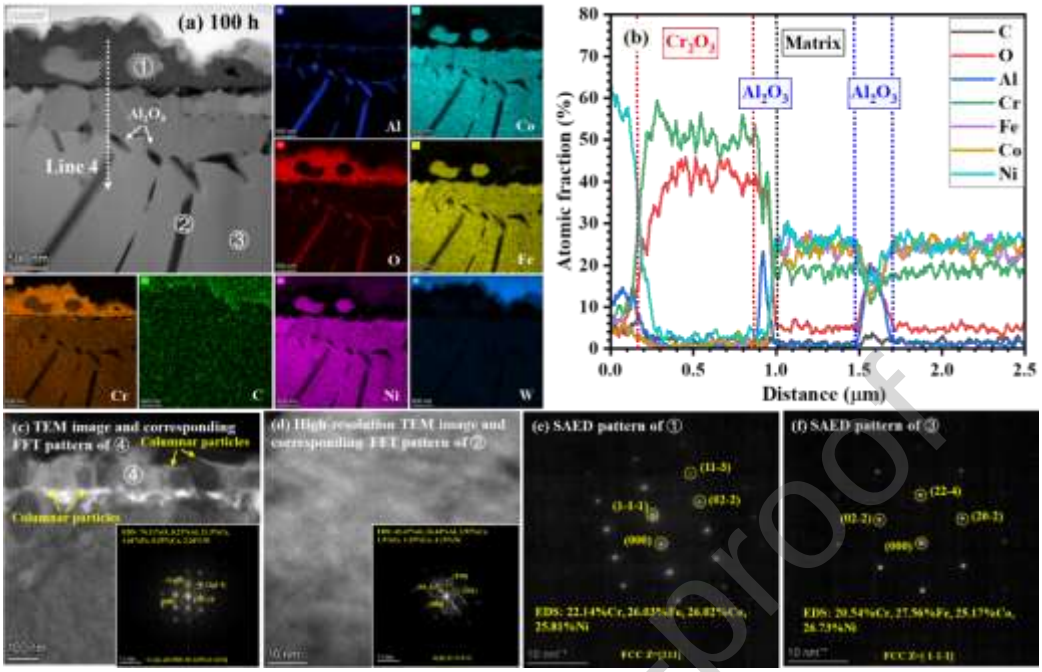

Figure 9 TEM analysis of the cross-section of the oxide film developed on $Al_{0.1}CoCrFeNi$ HEA after 100 h of exposure at 850 °C CO_2: (a) TEM image and corresponding EDS mapping, (b) the elemental EDS line (Line 4) scanning map of the oxide layer marked in the image (a); (c) TEM image and corresponding FFT pattern of the outer oxide layer; (d) high-resolution image and corresponding FFT pattern marked in the image (a); (e) and (f) SAED patterns of the positions marked in the image (a).

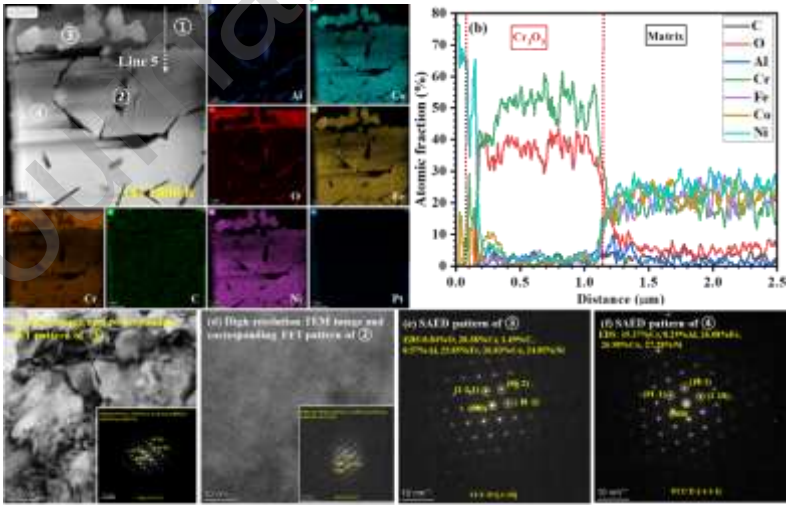

Figure 10 TEM analysis of the cross-section of the oxide film developed on $Al_{0.1}CoCrFeNi$ HEA after 1000 h of exposure at 850 °C CO_2: (a) TEM image and corresponding EDS mapping, (b) the elemental EDS line (Line 5) scanning map of the oxide layer marked in the image (a); (c) TEM image and FFT pattern of the outer oxide layer; (d) high-resolution image and corresponding FFT pattern marked in the image (a); (e) and (f) SAED patterns of the positions marked in the image (a).

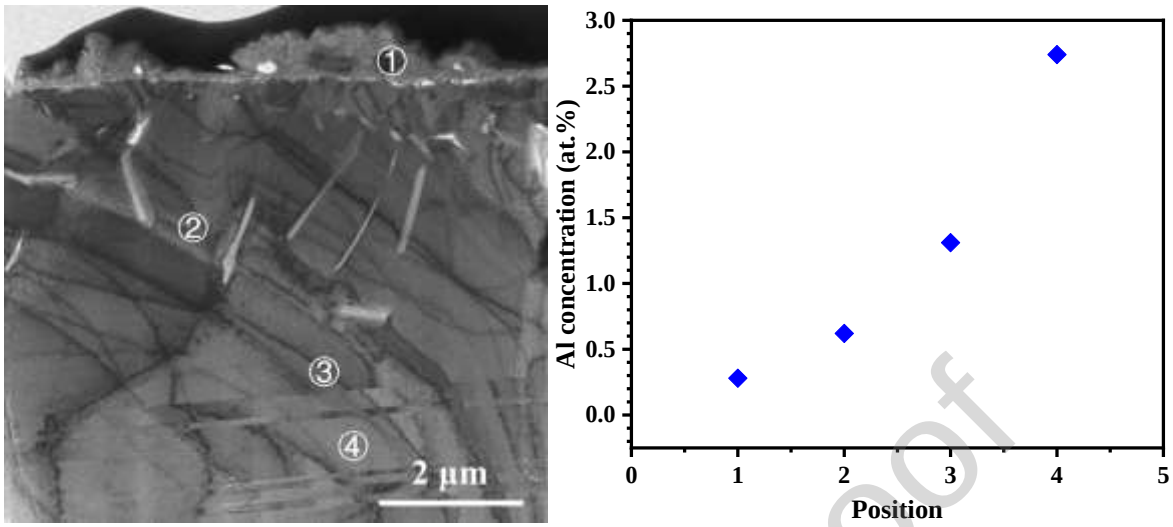

Figure 11 Al concentrations in $Al_{0.1}CoCrFeNi$ HEA and oxide film after 100 h of exposure at different positions.

Table 1 The chemical composition of the oxides developed on $Al_{0.1}CoCrFeNi$ HEA (at. %) after exposure to 850 °C high temperature CO_2 environment for different exposure periods.

Positions	O	Al	Cr	Fe	Co	Ni	Corresponding oxides
A	47.97	0.73	32.41	7.54	5.10	6.25	$(Cr_{0.62}Fe_{0.14}Al_{0.02}Co_{0.1}Ni_{0.12})_2O_3$
B	58.42	0.18	31.11	3.37	3.57	3.35	$(Cr_{0.75}Fe_{0.08}Co_{0.09}Ni_{0.08})_2O_3$
C	53.57	0.67	33.66	3.87	4.69	3.54	$(Cr_{0.72}Fe_{0.08}Al_{0.01}Co_{0.1}Ni_{0.08})_2O_3$
D	58.16	0.19	36.29	1.95	1.84	1.57	$(Cr_{0.87}Fe_{0.05}Co_{0.04}Ni_{0.04})_2O_3$
E	53.03	0.40	33.41	4.90	4.17	4.09	$(Cr_{0.71}Fe_{0.1}Al_{0.01}Co_{0.09}Ni_{0.09})_2O_3$
F	62.96	0.64	25.68	2.92	4.19	3.60	$(Cr_{0.69}Fe_{0.08}Al_{0.02}Co_{0.11}Ni_{0.1})_2O_3$

CRediT author contribution statement

Shanliang Zhou: Methodology, Investigation, Data Curation, Writing - Original draft preparation. **Zihang Liang:** Methodology, Data Curation**. Xi Huang:** Conceptualization, Methodology, Investigation, Resources, Supervision, Funding acquisition, Writing – Review & Editing. **Yuxuan Xia:** Methodology, Investigation, Data duration. **Qi Zhao**: Methodology, Data duration. **Chun Cheng:** Data duration. **Pengcheng Zhu:** Writing – Review & Editing. **Lu Wu:** Writing – Review & Editing. **Yujun Xie:** Conceptualization, Methodology, Investigation, Resources, Supervision, Funding acquisition, Writing – Review & Editing.

Declaration of Competing Interest

The authors declare that they have no known competing financial interests or personal relationships that could have appeared to influence the work reported in this paper.

Highlights

- The corrosion behavior of an FCC $Al_{0.1}CoCrFeNi$ HEA in high temperature carbon dioxide environment was investigated.
- A double-layer oxide film consisting of Cr_2O_3 and Al_2O_3 formed after 100 and 500 h of exposure, while a single layer of Cr_2O_3 developed after 1000 h of exposure.
- CoCrFeNi particles with an FCC structure were embedded in the oxide films irrespective of the exposure periods.
- A transition zone containing numerous striped-like Al_2O_3 oxides along the grain boundaries was formed underneath the Cr_2O_3 oxide films.